



FeNiP/MoO_x integrated electrode grown on monocrystalline NiMoO₄ nanorods with multi-interface for accelerating alkaline hydrogen evolution reaction

Zehao Xiao^a, Mei Yang^a, Jie Wang^d, Zonglin Xu^a, Shilin Zhang^a, Aidong Tang^{a,b,c,*}, Ruijie Gao^{b,c,*}, Huaming Yang^{b,c,d,*}

^a College of Chemistry and Chemical Engineering, Central South University, Changsha 410083, China

^b Engineering Research Center of Nano-Geomaterials of Ministry of Education, China University of Geosciences, Wuhan 430074, China

^c Faculty of Materials Science and Chemistry, China University of Geosciences, Wuhan 430074, China

^d Hunan Key Lab of Mineral Materials and Application, School of Minerals Processing and Bioengineering, Central South University, Changsha 410083, China



ARTICLE INFO

Keywords:

Self-supported catalysts
Metal phosphides
Hydrogen evolution reaction
Multi-interface
Alkaline media

ABSTRACT

Transition metal phosphides are promising candidates for alkaline hydrogen evolution reaction (HER), but the activation of H₂O molecule is deficient. We adopt an interface engineering strategy to synthesize a hierarchical FeNiP/MoO_x integrated electrode with multi-interface grown on monocrystalline NiMoO₄ nanorods. Such catalyst exhibits remarkable alkaline HER performance with a low overpotential of 97 mV at the current density of 100 mA cm⁻² and sustainable durability over 20 h. Experimental and theoretical results reveal that interfaces among Fe₂P, Ni₅P₄, and MoO_x can efficiently activate H₂O molecules and facilitate H desorption. Moreover, employing FeNiP/MoO_x/NiMoO₄/NF as a cathode, the cell voltage as low as 1.62 V to achieve a current density of 100 mA cm⁻², with admirable durability over 20 h for alkaline water splitting (1.0 M NaOH + 0.5 M NaCl). This work offers a new avenue to rationally design a 3D robust, cost-effective catalyst with multi-interface for large-scale practical hydrogen production.

1. Introduction

With rising concerns about energy shortages and the greenhouse impact caused by the rapid consumption of fossil fuels, there is a tremendous push to develop green and renewable energy sources [1–3]. Hydrogen has been regarded as a promising energy carrier because of its zero greenhouse gas emission and highest energy density (143 kJ g⁻¹) [4]. Overall, the water-splitting strategy is widely recognized as sustainable and environment-friendly energy conversion technology for efficient production of H₂ from resource-rich water/seawater [5,6]. So far, Pt-based materials are generally considered the most active catalysts for HER; however, natural paucity and high-cost properties limit their further large-scale applications [7,8]. Consequently, rational development of highly active HER catalysts based on cost-effective, non-noble, and earth-abundant elements to replace noble materials is still challenging.

Recently, various non-noble catalysts have been investigated as potential candidates for HER, such as metal carbides [9,10], nitrides [11,

12], phosphides [13–15], selenides [16–18], and sulfides [19–21]. Among them, transition metal phosphides (TMPs) are promising catalysts with great activity and higher stability for alkaline HER because the electronegative P atom acts as a base to trap the H^{*} [22,23]. Interface engineering strategy extensively employed to construct heterointerface with abundant active sites and flexible electronic structure, which is crucial for strengthening the HER activity [24]. On the other hand, TMPs catalysts with multiple heterointerfaces have been demonstrated to have a shallow proton adsorption energy (ΔG_{H^*}). Still, the high kinetic barrier is due to water adsorption and activation at the heterointerface [25,26]. It is generally believed that metal oxides are important sites for activating water [27,28]. Unfortunately, the H affinity of metal oxides is too strong, resulting in sluggish reaction kinetics [29]. Thus, a unique heterostructure catalyst consisting of metal oxides and TMPs with multi-interface is highly constructive. Furthermore, HER activity is also closely related to the bubble desorption rates especially 3D structure can easily facilitate charge transfer in a radial direction and expose more active sites to accelerate the bubble desorption rates [30,31].

* Corresponding authors at: Engineering Research Center of Nano-Geomaterials of Ministry of Education, China University of Geosciences, Wuhan 430074, China.
E-mail addresses: adtang@csu.edu.cn (A. Tang), gaoruijie@cug.edu.cn (R. Gao), hmyang@csu.edu.cn (H. Yang).

Based on the above consideration, we successfully synthesized a hierarchical FeNiP/MoO_x integrated electrode with multi-interface grown on monocrystalline NiMoO₄ nanorods by the interface engineering strategy. The FeNiP/MoO_x/NiMoO₄/NF catalyst exhibits remarkable HER performance with a low overpotential of 97 mV to reach the current density of 100 mA cm⁻² and long-time durability 1 M KOH aqueous. Benefiting from the high intrinsic activity and efficient electron transport, using FeNiP/MoO_x/NiMoO₄/NF as the cathode, the cell voltage is as low as 1.62 V to reach 100 mA cm⁻² together with excellent durability over 20 h for overall water splitting (1.0 M KOH + 0.5 M NaCl). Experimental and theoretical results reveal that interface between Fe₂P, Ni₅P₄, and MoO_x can efficiently activate H₂O molecules and facilitate the H desorption.

2. Experimental section

2.1. Chemicals

All of the chemicals used were analytical grade without further purification. Iron (III) nitrate nonahydrate [Fe(NO₃)₃·9H₂O, Sinopharm Chemical Reagent Co. Ltd]; sodium hypophosphite monohydrate (NaH₂PO₂·H₂O, Macklin Ltd); nickel nitrate hexahydrate [Ni(NO₃)₂·6H₂O, Guangdong Guanghua Sci-Tech Co. Ltd]; ammonium molybdate tetrahydrate [(NH₄)₂Mo₂O₇·4H₂O, Kaida Chemical Reagent Co. Ltd]; ammonium fluoride (NH₄F, Sinopharm Chemical Reagent Co. Ltd); urea [CO(NH₂)₂, Sinopharm Chemical Reagent Co. Ltd]; potassium hydroxide (KOH, Tianjin Damao Chemical Reagent Factory); hydrochloric acid (HCl, 36.0%, Chengdu Kelong Chemical Co. LTD) and Ni foams (NF, 1.5 mm in thick, areal density 320 g cm⁻², Kunshan Lvchuang Co. LTD) were used as received. De-ionized (DI, 18.2 Ω cm⁻¹) water was used for the preparation of standard solutions.

2.2. Preparation of electrocatalysts

2.2.1. Synthesis of NiMoO₄/NF precursor

The bare NF (1 cm × 4 cm) was immersed in 3 M HCl for 10 min by ultrasonic treatment to remove the surface oxide layer, then washed with ethanol and DI water several times. Subsequently, cleaning NF was placed into the solution of 1.2 mmol Ni(NO₃)₂·6H₂O and 0.4 mmol (NH₄)₂Mo₂O₇·4H₂O with 35 mL of DI water ultrasonic treatment for 30 min and transferred to 50 mL Teflon autoclave. Finally, the mixed solution was kept at 150 °C for 6 h. After cooling down to room temperature, the obtained yellow NiMoO₄/NF was taken out and washed with DI water several times and dried at 60 °C for 12 h.

2.2.2. Synthesis of FeNiP/MoO_x/NiMoO₄/NF and other contrast catalysts

A piece of cleaning NiMoO₄/NF (1 cm × 1 cm) was immersed into a given amount of Fe(NO₃)₃ solution (0.1 g mL⁻¹, 0.2 g mL⁻¹, 0.3 g mL⁻¹, 0.4 g mL⁻¹ and 0.5 g mL⁻¹) for 10 s and dried in the open air. Then Fe-NiMoO₄/NF was located downstream of a tube furnace and 1.5 g NaH₂PO₂ upstream at the atmosphere of N₂ gas flow. Afterward, the tube furnace was heated to 400 °C at a ramp rate of 5 °C min⁻¹ and maintained for 2 h. After the furnace naturally cooled down to room temperature, the obtained black FeNiP/MoO_x/NiMoO₄/NF sample was taken out and washed with DI water. The FeNiP/MoO_x/NiMoO₄/NF loading excluding NF is around 6.1 mg cm⁻². The different Fe/Ni atomic ratios were calculated by inductively coupled plasma-atomic emission spectrometry (ICP-MS) from the powder following ultrasonic treatment of obtained catalysts. Conspicuously, as shown in Fig. S1, such etching process closely relates to the atomic ratio of Fe/Ni. The HER activity of the obtained catalyst is substantially influenced by the Fe(NO₃)₃ concentration. For contrast, the FeNiP/NF catalyst was obtained solely from Fe(NO₃)₃ immersed NF using the same phosphorization strategy, whereas the same technique was used to obtain the NiP/MoO_x/NiMoO₄/NF catalyst as FeNiP/MoO_x/NiMoO₄/NF but without Fe(NO₃)₃ impregnating progress.

2.3. Materials characterization

A Bruker D8 focus diffractometer instrument collected X-ray diffraction (XRD) patterns (Cu K α radiation, scan rate 2° min⁻¹). A TESCAN MIRA3 characterized sample morphologies at 20 kV scanning electron microscopy (SEM) instrument, and their structures were further analyzed with a Talos F200X transmission electron microscopy (TEM) instrument. ICP-MS measured element contents on an Agilent 7700. In addition, X-ray photoelectron spectroscopy (XPS) data was collected to investigate the chemical composition and valence states through a Thermo Scientific K-Alpha spectrometer equipped with a monochromatic Al-K α X-ray source, and the referencing C 1s peak at 284.8 eV was used to calibrate the binding energy. Wetting contact angle was conducted on a contact angle meter (JY-82B Kruss DSA).

2.4. Electrochemical measurement

Electrochemical measurements were carried out by an electrochemical workstation (Ivium V54813 electrochemical analyzer, Ivium Instruments, Inc. Netherlands) using a standard three-electrode system. A graphite rod was used as the counter electrode, while Ag/AgCl electrode was used as the reference electrode, respectively. All potentials were further corrected with iR correction (except overall water splitting section) and converted to the reversible hydrogen electrode (RHE) according to the equation:

$$E_{RHE} = 0.1976 + 0.059 \times pH + E_{Ag/AgCl} \quad (1)$$

HER polarization curves were recorded by linear sweep voltammetry (LSV) with a scan rate of 2 mV s⁻¹. Electrochemical impedance spectra (EIS) were measured at the overpotential of 50 mV from 0.01 Hz to 100 kHz with an amplitude of 5 mV. Cyclic voltammetry (CV) curves recorded at different scan rates (10–50 mV s⁻¹) in the potential range from 0.14 V to 0.22 V (vs. RHE) were used to calculate the electrochemical double-layer capacitance (C_{dl}) and estimate the effective electrochemical surface area (ECSA). The durability test was evaluated by the chronopotentiometry (CP) measurement at 10 mA cm⁻² and 100 mA cm⁻² for 20 h.

3. Results and discussion

3.1. Catalyst synthesis and characterization

The synthesis of the self-supported FeNiP/MoO_x/NiMoO₄/NF catalyst is illustrated in Fig. 1a. On the surface of NF, NiMoO₄ nanorods were first uniformly grown by a reported hydrothermal method in the presence of (NH₄)₂Mo₂O₇ and Ni(NO₃)₂. Subsequently, as-obtained NiMoO₄ nanorods were treated by Fe(NO₃)₃ etching, followed by thermal phosphorization at 400 °C for 2 h with NaH₂PO₂ supplied at the upstream under N₂ protection. This synthesis process constructed a unique structure with multi-interface and fast electronic transport. As shown in Fig. S2, the formation of FeNiP/MoO_x/NiMoO₄/NF catalyst can be visually identified by the color change of silver-white NF to yellow NiMoO₄ to black after annealing.

SEM investigated the morphological and structural properties of as-prepared catalysts. As shown in Fig. S3, the surface of NF is smooth with a clear texture. After the hydrothermal, in-situ grown self-supported 3D hierarchical NiMoO₄ nanorods are highly dispersive and vertically stacked (Fig. S4). Followed by the Fe(NO₃)₃ etching and phosphorization, the FeNiP/MoO_x/NiMoO₄/NF catalyst remains nanorods structure (Figs. 1b and S5). The enlarged SEM image in Fig. 1c shows that many nanoparticles densely cover the surface of NiMoO₄ nanorods. These novel structures are in direct contact with nanorods, enabling efficient electron transport and increased exposure of active sites, which may play a vital role in promoting HER [32,33]. As shown in Fig. S6, many nanoparticles are uniformly distributed on the surface of NF after

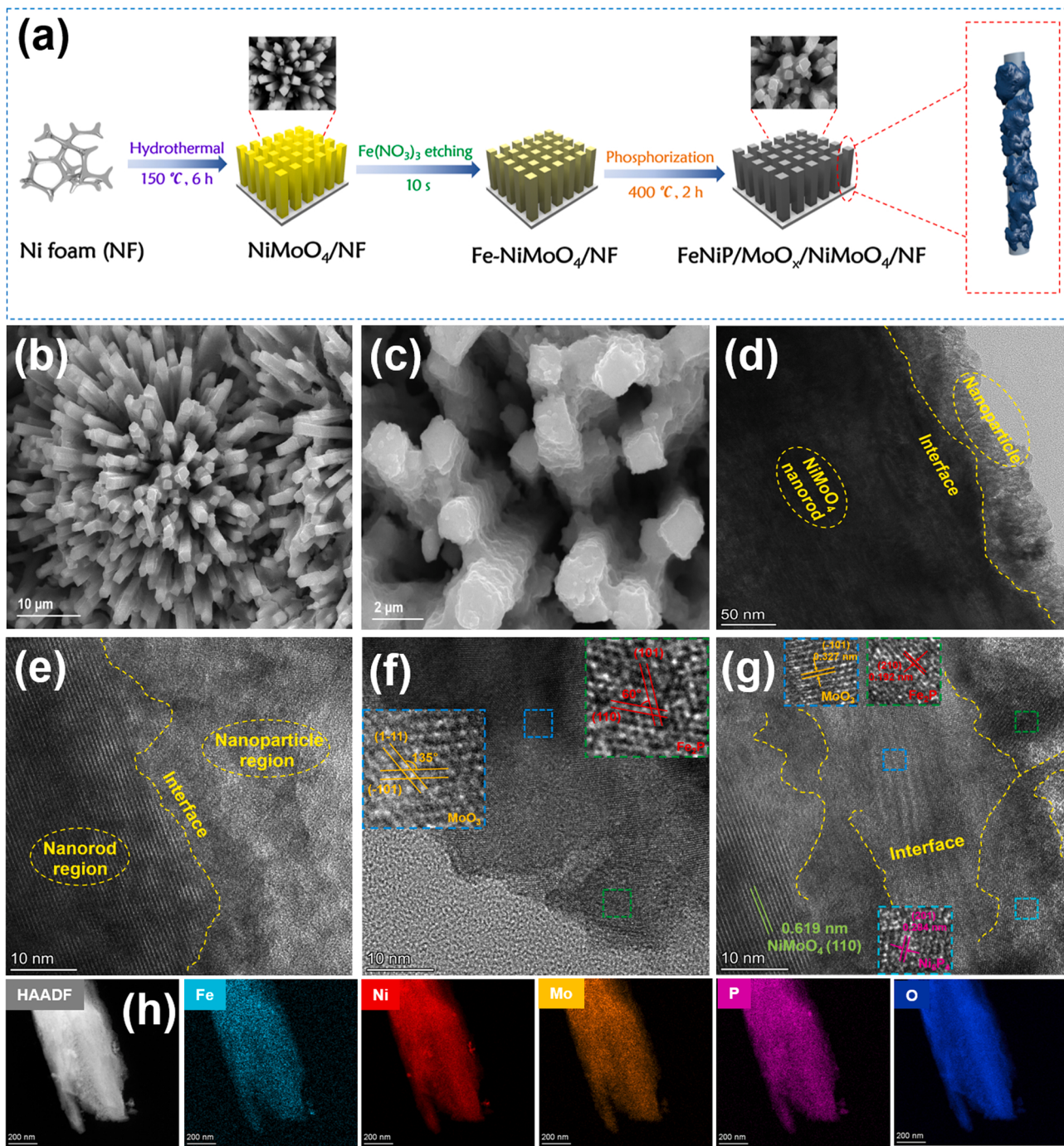


Fig. 1. Synthesis and microscopic characterization of the FeNiP/MoO_x/NiMoO₄/NF catalyst. (a) Schematic illustration of the synthetic route toward FeNiP/MoO_x/NiMoO₄/NF catalyst, (b, c) SEM images at different magnifications, (d) TEM image, (e–g) high-resolution TEM image, and (h) dark-field TEM image and the corresponding EDS elemental mapping of the FeNiP/MoO_x/NiMoO₄/NF catalyst.

phosphorization. Notably, there is no change on the surface of nanorods without etching after phosphorization in Fig. S7. TEM was employed to investigate the multi-interface of FeNiP/MoO_x/NiMoO₄/NF catalyst. Fig. 1d, e illustrates different interfaces between Ni/Fe phosphides and NiMoO₄ nanorods fitted using SEM results. Fig. 1f revealed that generation of copious interfaces between the lattice fringes 0.335 nm and 0.327 nm with intersection angle of 135.0° belong to (200) and (−101) planes of MoO₃, the lattice fringes of 0.286 and 0.293 nm with the intersection angle of 60.0° can be indexed to (101) and (110) planes of Fe₂P, respectively. As shown in Fig. 1g, the (110) plane of NiMoO₄ (JCPDS 33-0948) with 0.619 nm is observed, and lattice fringe of

0.327 nm belong to (−101) plane of MoO₃ (JCPDS 70-1035), while those of 0.284 and 0.192 nm distance are attributed to the (201) and (210) planes of Ni₅P₄ (JCPDS 18-0883) and Fe₂P (JCPDS 27-1171), respectively, which are further fitted by the corresponding selected area electron diffraction (SAED) pattern in Fig. S8. Prominently, great clear interfaces accompanied between the edges of Fe₂P, Ni₅P₄, MoO₃, and NiMoO₄ are observed in the HRTEM image. The energy dispersive spectroscopy (EDS) mapping indicates the high dispersion of Fe, Ni, Mo, P, and O in the FeNiP/MoO_x/NiMoO₄/NF catalyst (Fig. 1h). Moreover, the SAED pattern of a single NiMoO₄ nanorod indicates the obvious monocrystalline nature (Fig. S9), which can offer rapid transporting

paths for ions/electrons [34].

The chemical compositions of catalysts were further investigated. The typical XRD pattern of precursor indicates that vertical nanorods mainly consist of $\text{NiMoO}_4 \cdot x\text{H}_2\text{O}$ (Fig. S10). As shown in Fig. 2a, the XRD pattern of FeNiP/MoO_x/NiMoO₄/NF catalyst specifies the successful formation of Fe_2P , Ni_5P_4 , and MoO_3 components after the $\text{Fe}(\text{NO}_3)_3$ etching and subsequent phosphorization. The XPS survey spectrum confirms the presence of main elements Fe, Ni, Mo, P, and O in the FeNiP/MoO_x/NiMoO₄/NF catalyst (Fig. S11), which corresponds to the EDS results. The Fe 2p spectra (Fig. 2b) are divided into three spin-orbit doublets, corresponding to the Fe-P phase and Fe species (Fe^{2+} and Fe^{3+}) [35]. The Ni 2p spectra of FeNiP/MoO_x/NiMoO₄/NF catalyst displays three typical peaks in Fig. 2c, which are ascribed to Ni-P of Ni_5P_4 [35], Ni^{2+} in surface oxide, and a satellite peak [36,37]. The Mo 3d spectra of FeNiP/MoO_x/NiMoO₄/NF catalyst show two valence states of Mo⁶⁺ (231.55 eV) and Mo⁴⁺ (229.85 eV) in Fig. 2d, indicating reduction on a surface via annealing in PH_3 reduction atmosphere [38, 39]. In the P 2p area (Fig. 2e), the peaks at 128.6 and 129.5 eV are assigned to P 2p_{3/2} and P 2p_{1/2} of metal phosphides, respectively, whereas the other peak at 133.4 eV is attributed to the oxidized phosphorus species [40]. As shown in Fig. 2f, the O 1s spectra show two peaks correspond to M-O and P-O bonds [41,42]. In comparison to FeNiP/NF, the binding energies of Fe 2p and Ni 2p in FeNiP/MoO_x/NiMoO₄/NF catalysts are both shifted negatively 0.90 and 0.76 eV, respectively, while the peak of P 2p for the metal phosphide is shifted negatively 0.65 eV. These results suggest that more electrons accumulating around the metal phosphide after coupling with MoO_x to form a multi-interface [43]. Such charge redistribution is beneficial for optimizing intermediate adsorption/dissociation energies and decreasing the reaction energy barrier for H_2O activation, likely to enhance the catalytic performance.

3.2. Electrocatalytic evaluation

To evaluate the HER performance of FeNiP/MoO_x/NiMoO₄/NF catalyst, the electrochemical measurements using a standard three-electrode system were constructed in 1 M KOH. From LSV curves (Fig. 3a), FeNiP/MoO_x/NiMoO₄/NF catalyst shows an excellent HER activity with the low overpotential of 97 mV to reach at the current density of 100 mA cm⁻², lower than that of NiMoO_4 /NF (384 mV), NiP/MoO_x/NiMoO₄/NF (271 mV), FeNiP/NF (194 mV) and 20 wt% Pt/C/NF (139 mV). Additionally, Fig. S12 illustrates the HER activity of FeNiP/MoO_x/NiMoO₄/NF catalysts synthesized at various $\text{Fe}(\text{NO}_3)_3$ concentrations and 0.3 g mL⁻¹ of $\text{Fe}(\text{NO}_3)_3$ found an optimum concentration in the reactant. Tafel slopes were also determined by fitting the Tafel plots to the Tafel equation to determine the catalytic kinetics of HER (Fig. 3b) [44]. FeNiP/MoO_x/NiMoO₄/NF possesses a smaller Tafel slope of 21.2 mV dec⁻¹ than NiMoO_4 (129.5 mV dec⁻¹), NiP/MoO_x/NiMoO₄/NF (121.7 mV dec⁻¹), FeNiP/NF (100.1 mV dec⁻¹) and 20 wt % Pt/C/NF (48.5 mV dec⁻¹). It implies a conventional Volmer-Tafel mechanism, with the H_2 desorption (Tafel step) being the rate-determining step rather than the H_2O dissociation (Volmer step) [45,46]. Moreover, the FeNiP/MoO_x/NiMoO₄/NF catalyst exhibits better performance than recently reported phosphides/oxides HER catalysts with similar loading based on NF under the same 1.0 M KOH solution as shown in Fig. 3c and Table S1. The exchange current density (j_0) values of catalysts are calculated through the extrapolation of Tafel plots (Fig. S13). The j_0 value of FeNiP/MoO_x/NiMoO₄/NF (3.104 mA cm⁻²) higher than FeNiP/NF (1.315 mA cm⁻²) and NiP/MoO_x/NiMoO₄/NF (0.147 mA cm⁻²), which is instigated by the multi-interface structure of FeNiP/MoO_x/NiMoO₄/NF. The Nyquist plots demonstrate that FeNiP/MoO_x/NiMoO₄/NF (1.4 Ω) has a lower charge transferring resistance (R_{ct}) than FeNiP/NF (1.7 Ω) and NiP/MoO_x/NiMoO₄/NF (2.6 Ω), implying a greater electrical conductivity in HER (Fig. S14). The wetting contact angle of FeNiP/MoO_x/NiMoO₄/NF catalyst was measured (Fig. S15 and Movie S1). A drop of water was

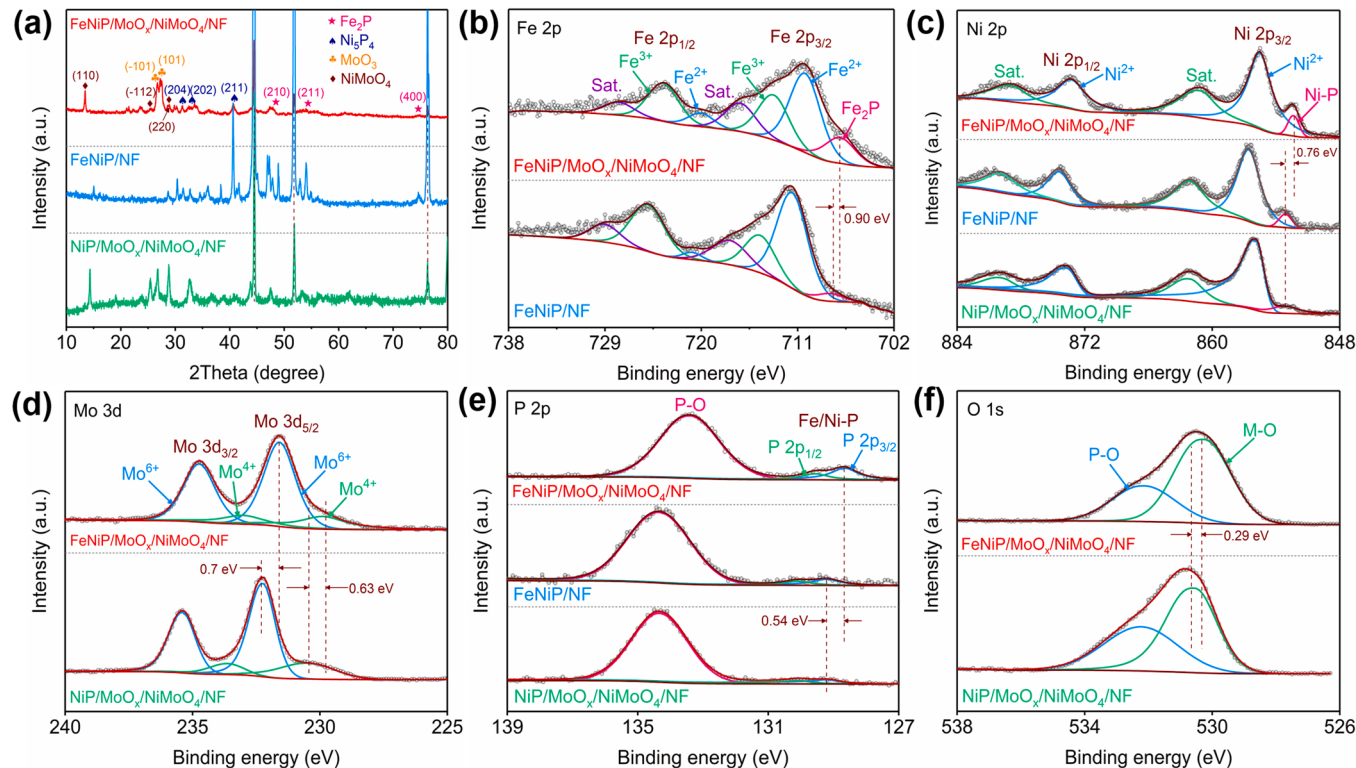


Fig. 2. Structural characterizations. (a) XRD patterns and high-resolution XPS spectra of (b) Fe 2p, (c) Ni 2p, (d) Mo 3d, (e) P 2p, and (f) O 1s of FeNiP/MoO_x/NiMoO₄/NF, FeNiP/NF and NiP/MoO_x/NiMoO₄/NF catalysts.

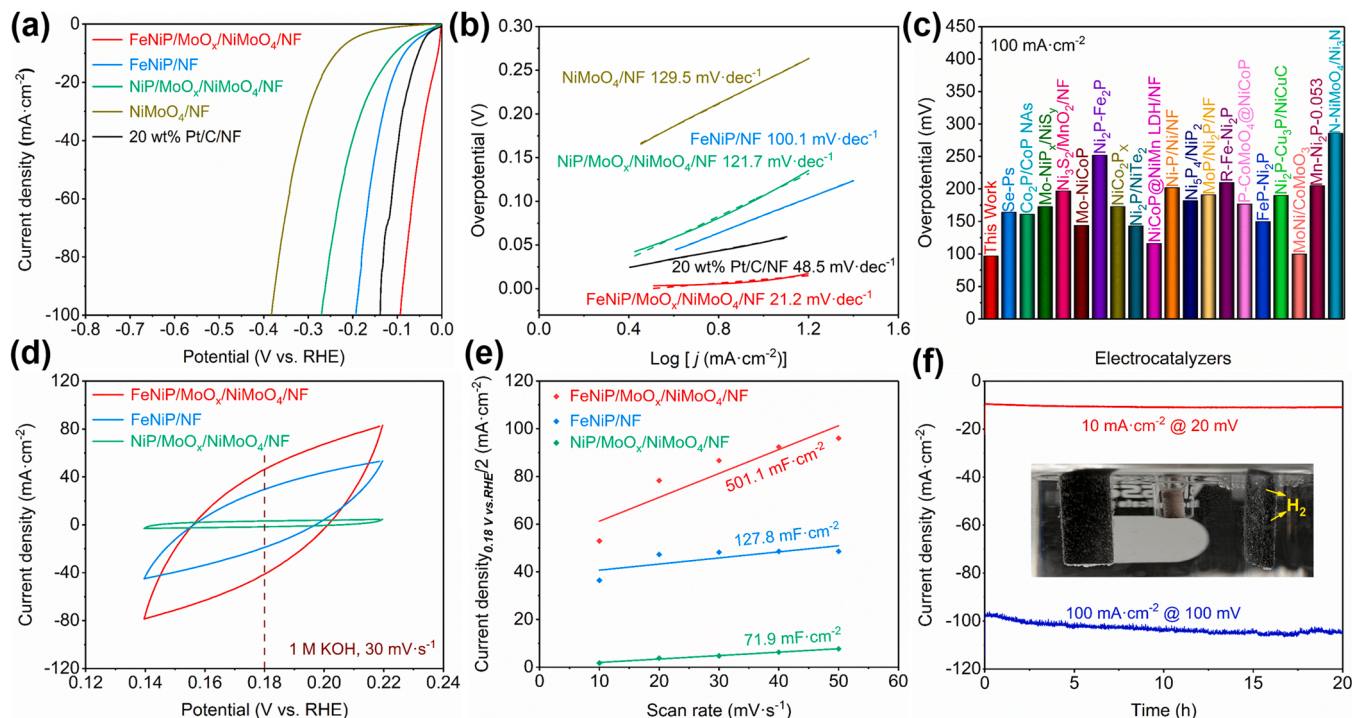


Fig. 3. Electrochemical HER measurements of various catalysts in 1 M KOH. (a) Polarization curves and (b) corresponding Tafel plots of NF, NiMoO₄/NF, FeNiP/NF, NiP/MoO_x/NiMoO₄/NF and FeNiP/MoO_x/NiMoO₄/NF catalysts. (c) Comparison of the overpotential required at a current density of 100 mA cm⁻² among our catalyst with reported HER catalysts. (d) CV curves of FeNiP/MoO_x/NiMoO₄/NF, FeNiP/NF, and NiP/MoO_x/NiMoO₄/NF at 30 mV s⁻¹ in the non-Faradaic capacitance current range and (e) linear dependence of capacitive current density at 0.18 V (vs. RHE) under different scan rates. (f) Durability tests of the FeNiP/MoO_x/NiMoO₄/NF catalyst at 10 and 100 mA cm⁻² (inset: the digital photo of HER catalyzed by the FeNiP/MoO_x/NiMoO₄/NF catalyst).

rapidly adsorbed on the surface of FeNiP/MoO_x/NiMoO₄/NF, indicating that more reactants in the electrolyte can readily come into touch with active surface sites, another essential factor in the notable catalytic activity.

Supplementary material related to this article can be found online at doi:10.1016/j.apcatb.2021.120913.

To understand the origin of HER performance of FeNiP/MoO_x/NiMoO₄/NF, a series of CV measurements were performed under scan rates varying from 10 m to 50 mV s⁻¹ (Figs. 3d and S16). In Fig. 3e, double-layer capacitance (C_{dl}) of different catalysts were measured in the non-Faraday region to estimate ECSA. FeNiP/MoO_x/NiMoO₄/NF has the highest C_{dl} value of 501.1 mF cm⁻², which is 3.92 and 6.97 times greater than FeNiP/NF (127.8 mF cm⁻²) and NiP/MoO_x/NiMoO₄/NF (71.9 mF cm⁻²), respectively, indicating the multi-interface provides abundant active sites for HER. As shown in Fig. S17, CV cycles of different catalysts under the scan rate of 30 mV s⁻¹ are used to analyze ECSA and further evaluate the effect of the corresponding Fe/Ni atomic ratio on the inherent activity. Markedly, 0.3 g mL⁻¹ of Fe(NO₃)₃ also found an optimum concentration in the reactant. In addition, the specific activity normalized by ECSA is plotted in Fig. S18, showing FeNiP/MoO_x/NiMoO₄/NF still executes better than NiP/MoO_x/NiMoO₄/NF and FeNiP/NF. The turnover frequency (TOF) gives the number of hydrogen molecules generated per second per active site to index the intrinsic catalytic activity [47,48]. The TOF value of FeNiP/MoO_x/NiMoO₄/NF is 0.844 s⁻¹ at 50 mV, as shown in Fig. S19, which is higher than FeNiP/NF and NiP/MoO_x/NiMoO₄/NF, which are 0.365 and 0.457 s⁻¹, respectively. The durability of FeNiP/MoO_x/NiMoO₄/NF was further tested (Fig. 3f and Movie S2), large amounts of bubbles rapidly overflow from the electrode surface, and CP curves exhibit great stability for over 20 h of alkaline HER at constant 10 and 100 mA cm⁻². Furthermore, the LSV curve reveals a minor shift after the long-term stability test (Fig. S20). Both structures have no visible change, demonstrating the good catalytic durability and chemical composition

established by SEM, XRD, and XPS analyses (Figs. S21–S23).

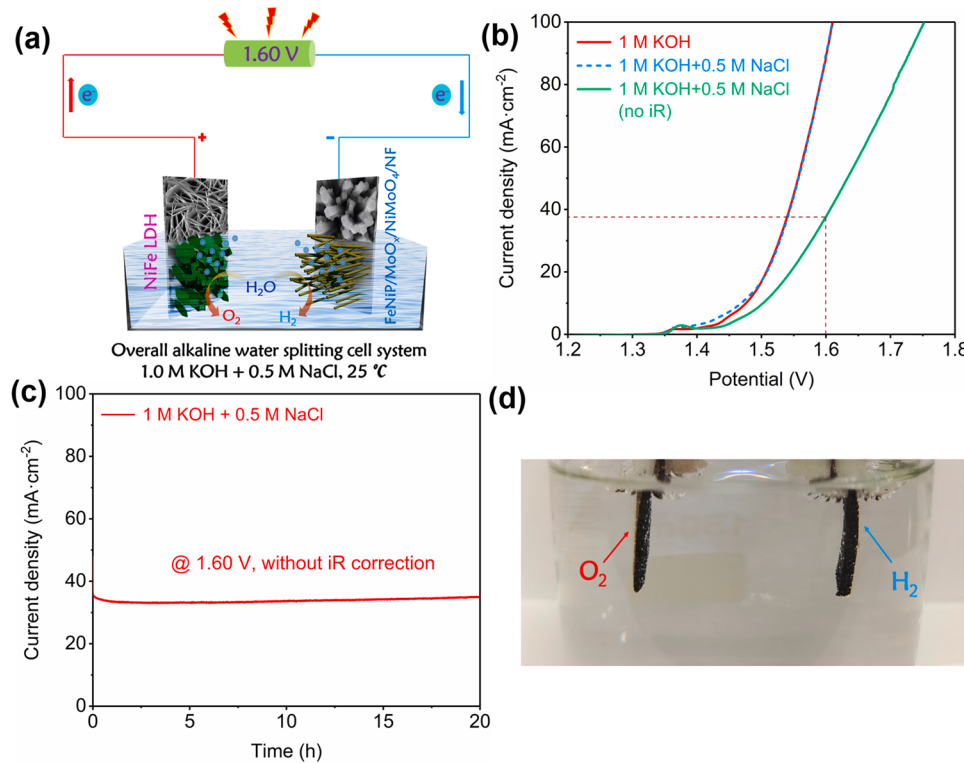
Supplementary material related to this article can be found online at doi:10.1016/j.apcatb.2021.120913.

Encouraged by excellent alkaline HER activity of FeNiP/MoO_x/NiMoO₄/NF catalyst, we established an overall water splitting cell system by using FeNiP/MoO_x/NiMoO₄/NF and NiFe LDH as a cathode and an anode to investigate their overall water splitting performance in 1 M KOH and 1 M KOH + 0.5 M NaCl (Fig. 4a). NiFe LDH nanosheets catalysts were synthesized by a reported hydrothermal method (Figs. S24 and S25) [49]. As shown in Fig. S26 and S27, both NiFe LDH nanosheets and FeNiP/MoO_x/NiMoO₄/NF exhibit excellent OER and HER activity in 1 M KOH and 1 M KOH + 0.5 M NaCl. According to the LSV curves in Fig. 4b, the FeNiP/MoO_x/NiMoO₄/NF(–) || NiFe LDH(+) cell system requires low voltages of 1.47 V and 1.62 V to achieve overall water splitting (1.0 M KOH + 0.5 M NaCl) of 10 and 100 mA cm⁻². To evaluate the cell system stability, a continuous operation for 20 h under 1.60 V without iR correction (Fig. 4c) shows negligible degradation of current density, revealing its excellent electrochemical stability, indicating the excellent appropriateness for practical large-scale applications. As shown in Fig. 4d and Movie S3, continuous release of gas bubbles rapidly generates on both electrodes. In a summary, the FeNiP/MoO_x/NiMoO₄/NF(–) || NiFe LDH(+) cell system ensures an excellent design for overall practical water splitting application because of its high activity and long-term durability.

Supplementary material related to this article can be found online at doi:10.1016/j.apcatb.2021.120913.

3.3. DFT calculations

To further study the HER mechanism of FeNiP/MoO_x/NiMoO₄ catalyst, density functional theory (DFT) calculations were performed to evaluate the adsorption free energies of water and hydrogen for alkaline HER. The model of MoO_x, Ni₅P₄/MoO_x, FeNiP/MoO_x, Ni₅P₄/NiMoO₄,



and Fe₂P/NiMoO₄ were built (Fig. 5a–e). As shown in Fig. 5f and Table S2, MoO_x is inert for the adsorption of H₂O molecules; however, the surface of Ni₅P₄/MoO_x heterostructure prefers adsorbing H₂O. Moreover, O vacancies on MoO_x may further facilitate the adsorption of H₂O and be beneficial for the activation of water. As for FeNiP/MoO_x, the water dissociation barrier is significantly decreased, indicating MoO_x coupled with Fe₂P-Ni₅P₄ can promote water activation and increase the rate of H^{*} formation. Nevertheless, NiMoO₄ linked is not an essential active site for H₂O molecules and H^{*} adsorption. As shown in Fig. 5g, in the subsequent Tafel step, the Fe₂P-Ni₅P₄ heterointerface acts as a vital H^{*} acceptor. It plays a key role in H₂ evolution because of its H^{*}

Fig. 4. Overall water splitting performance. (a) Schematic diagram of the 1.60 V driven overall water splitting cell system at room temperature. (b) Polarization curves of the FeNiP/MoO_x/NiMoO₄/NF (–) || NiFe LDH (+) cell system for overall water splitting in 1 M KOH and 1 M KOH + 0.5 M NaCl. (c) Durability test at a cell voltage of 1.60 V for the FeNiP/MoO_x/NiMoO₄/NF (–) || NiFe LDH (+) cell system without iR correction. (d) Digital image of overall water splitting cell system under 1.60 V.

adsorption energy (−0.04 eV), which is better than Pt [50,51]. As expected, our study shows that the electrical interaction impact of multi-interface between Fe₂P-Ni₅P₄ heterointerface with MoO_x is favorable for enhanced HER activity. According to the above-performed experiments and DFT analysis, the FeNiP/MoO_x/NiMoO₄/NF catalytic mechanism is depicted in Fig. 6, where Fe₂P-Ni₅P₄ and Fe₂P/MoO_x are responsible for Tafel step and Volmer step, respectively, this combination can significantly facilitate the alkaline HER activity.

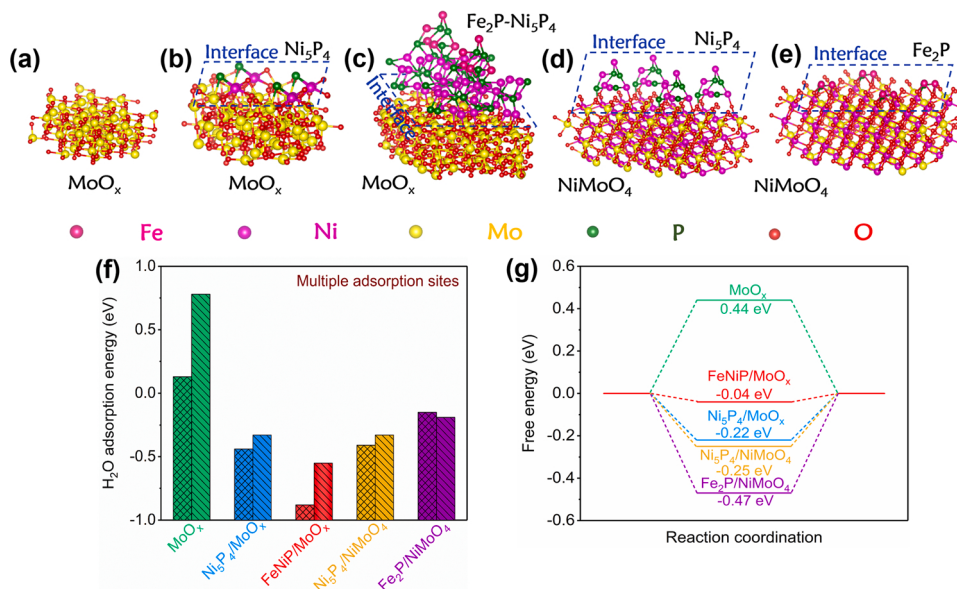


Fig. 5. DFT calculations. (a–e) Schematic models of MoO_x, Ni₅P₄/MoO_x, FeNiP/MoO_x, Ni₅P₄/NiMoO₄ and Fe₂P/NiMoO₄. (f) Free energy diagrams of water adsorption and (g) adsorption of H^{*} on the surface of MoO_x, Ni₅P₄/MoO_x, FeNiP/MoO_x, Ni₅P₄/NiMoO₄, and Fe₂P/NiMoO₄.

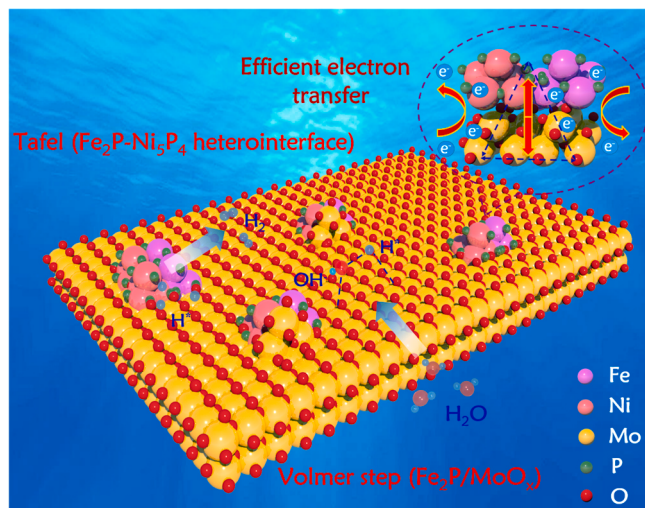


Fig. 6. The enhanced mechanism of the FeNiP/MoO_x/NiMoO₄/NF catalyst for alkaline HER by constructing bifunctional active structures.

4. Conclusions

In summary, we reported a hierarchical FeNiP/MoO_x/NiMoO₄/NF integrated electrode with multi-interface grown on monocrystalline NiMoO₄ nanorods by the interface engineering strategy, which is highly efficient for accelerating alkaline hydrogen production. Such FeNiP/MoO_x/NiMoO₄/NF catalyst shows outstanding HER performances in alkaline conditions with an extremely low overpotential of 97 mV at the current density of 100 mA cm⁻², significantly outperforming the most reported efficient catalysts. In addition, using FeNiP/MoO_x/NiMoO₄/NF as a cathode, the operating voltage is as low as 1.62 V to reach the current density of 100 mA cm⁻² with excellent durability over 20 h for overall water splitting. Both experimental and theoretical results reveal that the Fe₂P-Ni₅P₄ heterointerface coupling with MoO_x to form a multi-interface structure can efficiently activate H₂O molecules and facilitate the H desorption. This work offers a new avenue to rationally design a 3D robust, cost-effective catalyst with multi-interface for large-scale practical hydrogen production.

CRediT authorship contribution statement

Zehao Xiao: Conceptualization, Methodology, Visualization, Formal analysis, Writing – original draft, Investigation, Data curation. **Mei Yang:** Formal analysis, Investigation, Data curation. **Jie Wang:** Software, Visualization. **Zonglin Xu:** Formal analysis, Resources. **Shilin Zhang:** Formal analysis. **Aidong Tang:** Writing – review & editing, Funding acquisition, Supervision. **Ruijie Gao:** Conceptualization, Writing – review & editing, Software, Supervision, Project administration. **Huaming Yang:** Writing – review & editing, Funding acquisition, Supervision, Project administration.

Declaration of Competing Interest

The authors declare that they have no known competing financial interests or personal relationships that could have appeared to influence the work reported in this paper.

Acknowledgments

We are greatly grateful for the financial support by the National Natural Science Foundation of China (No. 51674293), the Fundamental Research Funds for the Central Universities of Central South University (No. 1053320210832), the National Postdoctoral Program for Innovative Talents (No. BX2021276), China Postdoctoral Science Foundation

(No. 2020M682519) and the Fundamental Research Funds for the Central Universities, China University of Geosciences (Wuhan).

Appendix A. Supplementary material

Supplementary data associated with this article can be found in the online version at doi:10.1016/j.apcatb.2021.120913.

References

- [1] Z.W. Seh, J. Kibsgaard, C.F. Dickens, I. Chorkendorff, J.K. Norskov, T.F. Jaramillo, Combining theory and experiment in electrocatalysis: insights into materials design, *Science* 355 (2017) eaad4998.
- [2] J. Luo, Y. Liu, C. Feng, C. Fan, L. Tang, G. Zeng, L. Wang, J. Wang, X. Tang, Joint connection of experiment and simulation for photocatalytic hydrogen evolution: strength, weakness, validation and complementarity, *J. Mater. Chem. A* 9 (2021) 6749–6774.
- [3] Z. Wang, H. Wang, S. Ji, H. Wang, D.J.L. Brett, R. Wang, Design and synthesis of tremella-like Ni-Co-S flakes on co-coated cotton textile as high-performance electrode for flexible supercapacitor, *J. Alloy. Compd.* 814 (2020), 151789.
- [4] X. Yu, Z.Y. Yu, X.L. Zhang, Y.R. Zheng, Y. Duan, Q. Gao, R. Wu, B. Sun, M.R. Gao, G. Wang, S.H. Yu, “Superaerophobic” nickel phosphide nanoarray catalyst for efficient hydrogen evolution at ultrahigh current densities, *J. Am. Chem. Soc.* 141 (2019) 7537–7543.
- [5] Z. Pu, I.S. Amiini, R. Cheng, P. Wang, C. Zhang, S. Mu, W. Zhao, F. Su, G. Zhang, S. Liao, S. Sun, Single-atom catalysts for electrochemical hydrogen evolution reaction: recent advances and future perspectives, *Nano-Micro Lett.* 12 (2020).
- [6] C.-T. Dinh, A. Jain, F.P.G. de Arquer, P. De Luna, J. Li, N. Wang, X. Zheng, J. Cai, B. Z. Gregory, O. Voznyy, B. Zhang, M. Liu, D. Sinton, E.J. Crumlin, E.H. Sargent, Multi-site electrocatalysts for hydrogen evolution in neutral media by destabilization of water molecules, *Nat. Energy* 4 (2018) 107–114.
- [7] X. Zhang, F. Meng, S. Mao, Q. Ding, M.J. Shearer, M.S. Faber, J. Chen, R.J. Hamers, S. Jin, Amorphous MoS₂Cl_x electrocatalyst supported by vertical graphene for efficient electrochemical and photoelectrochemical hydrogen generation, *Energy Environ. Sci.* 8 (2015) 862–868.
- [8] Z. Chen, X. Duan, W. Wei, S. Wang, B.-J. Ni, Recent advances in transition metal-based electrocatalysts for alkaline hydrogen evolution, *J. Mater. Chem. A* 7 (2019) 14971–15005.
- [9] J.-Q. Chi, W.-K. Gao, J.-H. Lin, B. Dong, J.-F. Qin, Z.-Z. Liu, B. Liu, Y.-M. Chai, C.-G. Liu, Porous core-shell N-doped Mo₂C@C nanospheres derived from inorganic-organic hybrid precursors for highly efficient hydrogen evolution, *J. Catal.* 360 (2018) 9–19.
- [10] C.-F. Li, J.-W. Zhao, L.-j Xie, J.-Q. Wu, G.-R. Li, Water adsorption and dissociation promoted by Co⁺-N-C⁺-biactive sites of metallic Co/N-doped carbon hybrids for efficient hydrogen evolution, *Appl. Catal. B* 282 (2021), 119463.
- [11] G.-f Long, K. Wan, M.-y Liu, Z.-x Liang, J.-h Piao, P. Tsakaras, Active sites and mechanism on nitrogen-doped carbon catalyst for hydrogen evolution reaction, *J. Catal.* 348 (2017) 151–159.
- [12] J. Sun, W. Xu, C. Lv, L. Zhang, M. Shakouri, Y. Peng, Q. Wang, X. Yang, D. Yuan, M. Huang, Y. Hu, D. Yang, L. Zhang, Co/Mo hetero-interface nanoflake array with enhanced water dissociation capability achieves the Pt-like hydrogen evolution catalytic performance, *Appl. Catal. B* 286 (2021), 119882.
- [13] Y. Wen, J. Qi, D. Zhao, J. Liu, P. Wei, X. Kang, X. Li, O doping hierarchical NiCoP/Ni₂P hybrid with modulated electron density for efficient alkaline hydrogen evolution reaction, *Appl. Catal. B* 293 (2021), 120196.
- [14] J. Sun, M. Ren, L. Yu, Z. Yang, L. Xie, F. Tian, Y. Yu, Z. Ren, S. Chen, H. Zhou, Highly efficient hydrogen evolution from a mesoporous hybrid of nickel phosphide nanoparticles anchored on cobalt phosphosulfide/phosphide nanosheet arrays, *Small* 15 (2019), e1804272.
- [15] X. Zhang, F. Zhou, W. Pan, Y. Liang, R. Wang, General construction of molybdenum-based nanowire arrays for pH-universal hydrogen evolution electrocatalysis, *Adv. Funct. Mater.* 28 (2018) 1804600.
- [16] X.L. Zhang, S.J. Hu, Y.R. Zheng, R. Wu, F.Y. Gao, P.P. Yang, Z.Z. Niu, C. Gu, X. Yu, X.S. Zheng, C. Ma, X. Zheng, J.F. Zhu, M.R. Gao, S.H. Yu, Polymorphic cobalt diselenide as extremely stable electrocatalyst in acidic media via a phase-mixing strategy, *Nat. Commun.* 10 (2019) 5338.
- [17] B. Liu, Y.F. Zhao, H.Q. Peng, Z.Y. Zhang, C.K. Sit, M.F. Yuen, T.R. Zhang, C.S. Lee, W.J. Zhang, Nickel-cobalt diselenide 3D mesoporous nanosheet networks supported on Ni foam: an all-pH highly efficient integrated electrocatalyst for hydrogen evolution, *Adv. Mater.* 29 (2017) 1606521.
- [18] C. Liu, T. Gong, J. Zhang, X. Zheng, J. Mao, H. Liu, Y. Li, Q. Hao, Engineering Ni₂P-NiSe₂ heterostructure interface for highly efficient alkaline hydrogen evolution, *Appl. Catal. B* 262 (2020), 118245.
- [19] M. Ma, J. Xu, H. Wang, X. Zhang, S. Hu, W. Zhou, H. Liu, Multi-interfacial engineering of hierarchical CoNi₂S₄/WS₂/Co₉S₈ hybrid frameworks for robust all-pH electrocatalytic hydrogen evolution, *Appl. Catal. B* 297 (2021), 120455.
- [20] Y. Zhang, J. Fu, H. Zhao, R. Jiang, F. Tian, R. Zhang, Tremella-like Ni₃S₂/MnS with ultrathin nanosheets and abundant oxygen vacancies directly used for high speed overall water splitting, *Appl. Catal. B* 257 (2019), 117899.
- [21] Y. Xiong, L. Xu, C. Jin, Q. Sun, Interface-engineered atomically thin Ni₃S₂/MnO₂ heterogeneous nanoarrays for efficient overall water splitting in alkaline media, *Appl. Catal. B* 254 (2019) 329–338.

[22] A. Kumar, V.Q. Bui, J. Lee, A.R. Jadhav, Y. Hwang, M.G. Kim, Y. Kawazoe, H. Lee, Modulating interfacial charge density of $\text{NiP}_2\text{-FeP}_2$ via coupling with metallic Cu for accelerating alkaline hydrogen evolution, *ACS Energy Lett.* 6 (2021) 354–363.

[23] P. Xiao, W. Chen, X. Wang, A review of phosphide-based materials for electrocatalytic hydrogen evolution, *Adv. Energy Mater.* 5 (2015) 1500985.

[24] F. Du, L. Shi, Y. Zhang, T. Li, J. Wang, G. Wen, A. Alsaedi, T. Hayat, Y. Zhou, Z. Zou, Foam-like $\text{Co}_3\text{S}_8/\text{Ni}_3\text{S}_2$ heterostructure nanowire arrays for efficient bifunctional overall water-splitting, *Appl. Catal. B* 253 (2019) 246–252.

[25] Y. Liu, Q. Feng, W. Liu, Q. Li, Y. Wang, B. Liu, L. Zheng, W. Wang, L. Huang, L. Chen, X. Xiong, Y. Lei, Boosting interfacial charge transfer for alkaline hydrogen evolution via rational interior Se modification, *Nano Energy* 81 (2021).

[26] P. Xiao, M.A. Sk, L. Thia, X. Ge, R.J. Lim, J.-Y. Wang, K.H. Lim, X. Wang, Molybdenum phosphide as an efficient electrocatalyst for the hydrogen evolution reaction, *Energy Environ. Sci.* 7 (2014) 2624–2629.

[27] M.R. Gao, Y.F. Xu, J. Jiang, Y.R. Zheng, S.H. Yu, Water oxidation electrocatalyzed by an efficient $\text{Mn}_3\text{O}_4/\text{CoSe}_2$ nanocomposite, *J. Am. Chem. Soc.* 134 (2012) 2930–2933.

[28] Y.F. Xu, M.R. Gao, Y.R. Zheng, J. Jiang, S.H. Yu, Nickel/nickel(II) oxide nanoparticles anchored onto cobalt (IV) diselenide nanobelts for the electrochemical production of hydrogen, *Angew. Chem. Int. Ed.* 52 (2013) 8546–8550.

[29] T.Y. Ma, Y. Zheng, S. Dai, M. Jaroniec, S.Z. Qiao, Mesoporous MnCo_2O_4 with abundant oxygen vacancy defects as high-performance oxygen reduction catalysts, *J. Mater. Chem. A* 2 (2014) 8676–8682.

[30] Z. Zeng, G. Fu, H.B. Yang, Y. Yan, J. Chen, Z. Yu, J. Gao, L.Y. Gan, B. Liu, P. Chen, Bifunctional N-CoSe₂/3D-MXene as highly efficient and durable cathode for rechargeable Zn-air battery, *ACS Mater. Lett.* 1 (2019) 432–439.

[31] E. Pomerantseva, F. Bonaccorso, X. Feng, Y. Cui, Y. Gogotsi, Energy storage: the future enabled by nanomaterials, *Science* 366 (2019) eaan8285.

[32] S. Li, C. Yu, J. Yang, C. Zhao, M. Zhang, H. Huang, Z. Liu, W. Guo, J. Qiu, A superhydrophilic “nanoglue” for stabilizing metal hydroxides onto carbon materials for high-energy and ultralong-life asymmetric supercapacitors, *Energy Environ. Sci.* 10 (2017) 1958–1965.

[33] A. Sivanantham, P. Ganesan, S. Shanmugam, Hierarchical NiCo_2S_4 nanowire arrays supported on Ni foam: an efficient and durable bifunctional electrocatalyst for oxygen and hydrogen evolution reactions, *Adv. Funct. Mater.* 26 (2016) 4661–4672.

[34] Y.-J. Gu, W. Wen, S. Zheng, J.-M. Wu, Monocrystalline FeMnO_3 on carbon cloth for extremely high-areal-capacitance supercapacitors, *ACS Appl. Energy Mater.* 3 (2020) 11863–11872.

[35] L. Wu, L. Yu, F. Zhang, B. McElhenney, D. Luo, A. Karim, S. Chen, Z. Ren, Heterogeneous bimetallic phosphide $\text{Ni}_2\text{P}\text{-Fe}_2\text{P}$ as an efficient bifunctional catalyst for water/seawater splitting, *Adv. Funct. Mater.* 31 (2020) 2006484.

[36] M. Jin, X. Zhang, R. Shi, Q. Lian, S. Niu, O. Peng, Q. Wang, C. Cheng, Hierarchical $\text{CoP@Ni}_2\text{P}$ catalysts for pH-universal hydrogen evolution at high current density, *Appl. Catal. B* 296 (2021), 120350.

[37] J. Zhang, Z. Zhang, Y. Ji, J. Yang, K. Fan, X. Ma, C. Wang, R. Shu, Y. Chen, Surface engineering induced hierarchical porous $\text{Ni}_1\text{P}_2\text{S}_3\text{-Ni}_2\text{P}$ polymorphs catalyst for efficient wide pH hydrogen production, *Appl. Catal. B* 282 (2021), 119609.

[38] Z. Wang, J. Lu, S. Ji, H. Wang, X. Wang, B.G. Pollet, R. Wang, Integrating Ni nanoparticles into MoN nanosheets form Schottky heterojunctions to boost its electrochemical performance for water electrolysis, *J. Alloy. Compd.* 867 (2021), 158983.

[39] W. Hua, H. Sun, H. Liu, Y. Li, J.-G. Wang, Interface engineered $\text{NiMoN/Ni}_3\text{N}$ heterostructures for enhanced alkaline hydrogen evolution reaction, *Appl. Surf. Sci.* 540 (2021), 148407.

[40] X. Cheng, Z. Pan, C. Lei, Y. Jin, B. Yang, Z. Li, X. Zhang, L. Lei, C. Yuan, Y. Hou, A strongly coupled 3D ternary $\text{Fe}_2\text{O}_3\text{@Ni}_2\text{P/Ni}(\text{PO}_3)_2$ hybrid for enhanced electrocatalytic oxygen evolution at ultra-high current densities, *J. Mater. Chem. A* 7 (2019) 965–971.

[41] Y. Yan, B.Y. Xia, X. Ge, Z. Liu, A. Fisher, X. Wang, A flexible electrode based on iron phosphide nanotubes for overall water splitting, *Chem. Eur. J.* 21 (2015) 18062–18067.

[42] C.Y. Cao, J. Qu, W.S. Yan, J.F. Zhu, Z.Y. Wu, W.G. Song, Low-cost synthesis of flowerlike $\alpha\text{-Fe}_2\text{O}_3$ nanostructures for heavy metal ion removal: adsorption property and mechanism, *Langmuir* 28 (2012) 4573–4579.

[43] Y. Li, H. Zhang, M. Jiang, Q. Zhang, P. He, X. Sun, 3D self-supported Fe-doped Ni_2P nanosheet arrays as bifunctional catalysts for overall water splitting, *Adv. Funct. Mater.* 27 (2017) 1702513.

[44] T. Li, Y. Hu, X. Pan, J. Yin, Y. Li, Y. Wang, Y. Zhang, H. Sun, Y. Tang, N-carbon supported hierarchical $\text{Ni/Ni}_{0.2}\text{Mo}_{0.8}\text{N}$ nanosheets as high-efficiency oxygen evolution electrocatalysts, *Chem. Eng. J.* 392 (2020), 124845.

[45] J.X. Feng, J.Q. Wu, Y.X. Tong, G.R. Li, Efficient hydrogen evolution on Cu nanodots-decorated Ni_3S_2 nanotubes by optimizing atomic hydrogen adsorption and desorption, *J. Am. Chem. Soc.* 140 (2018) 610–617.

[46] K.L. Zhou, Z. Wang, C.B. Han, X. Ke, C. Wang, Y. Jin, Q. Zhang, J. Liu, H. Wang, H. Yan, Platinum single-atom catalyst coupled with transition metal/metal oxide heterostructure for accelerating alkaline hydrogen evolution reaction, *Nat. Commun.* 12 (2021) 3783.

[47] J. Kibsgaard, T.F. Jarlamio, F. Besenbacher, Building an appropriate active-site motif into a hydrogen-evolution catalyst with thiomolybdate $[\text{Mo}_3\text{S}_{13}]^{2-}$ clusters, *Nat. Chem.* 6 (2014) 248–253.

[48] J. Sun, F. Tian, F. Yu, Z. Yang, B. Yu, S. Chen, Z. Ren, H. Zhou, Robust hydrogen-evolving electrocatalyst from heterogeneous molybdenum disulfide-based catalyst, *ACS Catal.* 10 (2019) 1511–1519.

[49] C. Liu, Y. Han, L. Yao, L. Liang, J. He, Q. Hao, J. Zhang, Y. Li, H. Liu, Engineering bimetallic NiFe-based hydroxides/selenides heterostructure nanosheet arrays for highly-efficient oxygen evolution reaction, *Small* 17 (2021), e2007334.

[50] Y. Li, X. Tan, H. Tan, H. Ren, S. Chen, W. Yang, S.C. Smith, C. Zhao, Phosphine vapor-assisted construction of heterostructured $\text{Ni}_2\text{P}/\text{NiTe}_2$ catalysts for efficient hydrogen evolution, *Energy Environ. Sci.* 13 (2020) 1799–1807.

[51] X. Huang, X. Xu, X. Luan, D. Cheng, CoP nanowires coupled with CoMoP nanosheets as a highly efficient cooperative catalyst for hydrogen evolution reaction, *Nano Energy* 68 (2020), 104332.